M. Greiner
Professor of Mechanical Engineering,
University of Nevada,
Reno, Nevada 89557
e-mail: greiner@unr.edu

P. F. Fischer
Mathematics and Computer Science Division,
Argonne National Laboratory,
Argonne, IL 60439

H. M. Tufo
Department of Computer Science,
University of Chicago,
Chicago, IL 60637

R. A. Wirtz
Professor of Mechanical Engineering,
University of Nevada,
Reno, Nevada 89557

Three-Dimensional Simulations of Enhanced Heat Transfer in a Flat Passage Downstream From a Grooved Channel

Navier-Stokes simulations of three-dimensional flow and augmented convection in a flat passage downstream from a fully developed channel with symmetric, transverse grooves on two opposite walls were performed for 405≤Re≤764 using the spectral element technique. Unsteady flow that develops in the grooved region persists several groove-lengths into the flat passage, increasing both local heat transfer and pressure gradient relative to that in a steady flat passage. Moreover, the heat transfer for a given pumping power in the first three groove-lengths of the flat passage was greater than the levels observed in a fully developed grooved passage. [DOI: 10.1115/1.1418371]

Keywords: Augmentation, Computational, Forced Convection, Heat Transfer, Three-Dimensional

Introduction

Engineering devices frequently employ enhanced heat transfer surfaces [1]. Fins are typically used to extend surface areas while offset strips are commonly used to promote thin boundary layers. In recent years, a number of configurations that increase fluid mixing by triggering flow instabilities have been considered. Transversely grooved channels [2–4], passages with eddy promoters [5,6] and communicating channels [7] all contain fairly large features whose sizes are roughly half the channel wall to wall spacing. These structures are designed to excite normally damped Tollmien-Schlichting waves at moderately low Reynolds numbers.

The current authors have presented a series of articles on heat transfer augmentation in rectangular cross section passages with transverse grooves cut into the walls. Flow visualizations in a long contiguously grooved passage exhibit two-dimensional waves at a Reynolds number of Re=350, followed by a rapid transition to three-dimensional mixing [8]. Heat transfer and friction factor measurements using air show that both the Nusselt number and friction factor are greater than the corresponding values for a flat channel with the same minimum wall to wall spacing [9,10]. A significant result is that fully developed heat transfer is enhanced relative to laminar flat channel flow by as much as a factor of 4.6 at equal Reynolds numbers and by a factor of 3.5 at equal pumping powers. Three-dimensional numerical simulations for Re≤2000 give results that are in good agreement with experimental measurements [11,12]. Moreover, *two*-dimensional simulations were inadequate to capture the transport processes in these configurations for Reynolds numbers greater than Re=570.

Investigations of external flow heat transfer on flat surfaces *downstream* from disturbances have also shown favorable performance characteristics. For example, measurements made on a flat plate downstream from different turbulence-generating grids show that the ratio of heat transfer to friction factor increases linearly with increasing turbulence intensity [13]. Maciejewski and Moffat [14] measured heat transfer from a flat plate subject to very high levels of free-stream turbulence. Their measured heat transfer coefficients, along with that of Blair, increase linearly with the maximum turbulence intensity of the flow.

Experimental measurements in a flat passage downstream of a grooved channel were performed to determine the effect of decaying unsteadiness in an internal flow for the Reynolds number range 1500≤Re≤5000 [15]. These measurements show that the heat transfer coefficient remained high for a substantial distance in the flat region. The pressure gradient, on the other hand, dropped back to the flat passage value much more rapidly, especially for Re>2500. As a result, the heat transfer for a given pumping power was even greater in the first five hydraulic diameters of the decay region than in the grooved passage itself. Moreover, this uncoupled heat/momentum transport behavior suggests that intermittently grooved passages, in which flat regions separate contiguous grooved sections, may have significant advantages in engineering heat transfer devices.

The current work is a numerical investigation of heat and momentum transport in a flat plate passage downstream from a fully developed, symmetrically grooved channel with constant temperature surfaces. This simulation employs two different three-dimensional sub-domains. The first represents one periodicity cell of a continuously grooved passage. It has periodic inflow/outflow boundary conditions in order to simulate fully developed flow. The second subdomain consists of a single groove cell coupled to a flat passage at its downstream end. The inflow conditions to the grooved/flat sub-domain are taken from the outflow of the fully developed domain. The variations of centerline velocity unsteadiness, heat transfer coefficient and pressure gradient with axial position are presented for the Reynolds number range 405≤Re≤764. Heat transfer results from the current work are directly compared to experimental data [10,16]. Finally, the heat transfer versus pumping power performance of the first few groove lengths of the flat passage is compared to that of a fully developed groove channel.

Numerical Method

Computational Domain. Figure 1 shows the pair of three-dimensional sub-domains employed in this work. The upper and lower boundaries are solid walls, and the fluid flows from left to right (in the positive *x*-direction). The domain shown in Fig. 1(*a*) represents one periodicity cell of a long, symmetrically grooved

Contributed by the Heat Transfer Division for publication in the JOURNAL OF HEAT TRANSFER. Manuscript received by the Heat Transfer Division May 17, 2000; revision received June 15, 2001. Associate Editor: J. G. Georgiadis.

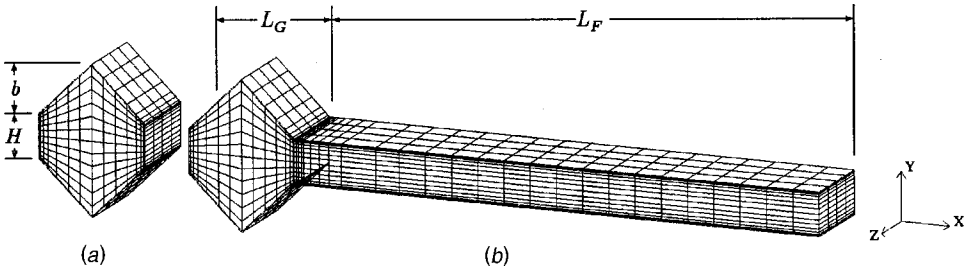

Fig. 1 Spectral element mesh. (*a*) Periodic groove domain. (*b*) Groove/flat domain. The *z*-direction width of both domains is *W*.

channel. The groove depth $b=1.2$ cm, groove length $L_G=2.4$ cm, and minimum wall-to-wall spacing $H=1.0$ cm are the same as those used in earlier experimental work [10,16]. These dimensions are chosen to be compatible with the wavelength of the most slowly decaying Tollmien-Schlichting waves of the outer channel flow [2]. This domain uses periodic inlet/outlet boundary conditions to model fully developed flow. Our earlier numerical simulations show that a single groove cell with periodic boundary conditions is sufficient to model heat transfer and pressure gradient to within 20 percent of experimentally measured values [12].

The sub-domain shown in Fig. 1(*b*) consists of a single groove coupled with a flat region at its downstream end. The flat region wall-to-wall spacing is $H=1.0$ cm and its length is $L_F=5L_G$. The conditions at the outlet of the periodic groove sub-domain (Fig. 1(*a*)) are used as the inlet conditions to the groove-flat domain. The outflow boundary condition for the groove-flat domain is the standard Neumann condition on velocity, $du/dx=0$. This condition produces a minimal flow-direction boundary layer having thickness and amplitude $O(1/\mathrm{Re})$ near the outlet. The grooved portion of the groove-flat domain is included so that the simulation models elliptic (upstream) effects caused by the flat passage. We refer to this region as the ''final'' or ''last'' groove since it represents the last groove before the flat passage. Periodic boundary conditions are imposed in the spanwise direction of both computational domains, for which the domain extent is $W=2.0$ cm.

The computational grids in both sub-domains consist of four levels in the *z*-direction. Each level of the periodic groove domain contains $K_P=196$ hexahedral spectral elements while the groove-flat domain has $K_{GF}=560$ elements in each *z*-level. In the spectral element method [17,18], the solution, data and geometric mapping are expressed as tensor-product polynomials of degree N in each spatial direction, corresponding to a total grid point count of roughly $4(K_P+K_{GF})N^3$. Numerical convergence is achieved by increasing the spectral order N.

The present simulations use consistent approximation spaces for velocity and pressure, with pressure represented as polynomials of degree $N-2$ [18,19]. The momentum equations are advanced by first computing the convection term, followed by a linear Stokes solve in which the velocity field is projected onto a divergence-free space. The scheme is second-order accurate in time. Further details on this method can be found in [19].

The Periodic Domain. In the periodic domain the flow is driven from left to right by a time-varying body force per unit mass f_x. This force is determined so that the mass flow rate through the domain is invariant with time [20]. The thermal problem for the periodic domain requires careful treatment. If one simply specifies zero-temperature conditions on the walls then the solution eventually decays to zero. To produce the desired spatially fully developed state requires that the temperature profiles at the inlet and outlet be self-similar, i.e.,

$$T(x=L_G,y,z,t)=CT(x=0,y,z,t),$$

with $C<1$. The solution technique for computing the fully developed temperature field for constant temperature boundary conditions follows the analysis of Patankar et al. [21]. The energy equation, and associated initial and boundary conditions are

$$\frac{\partial T}{\partial t}+\overline{U}\cdot\nabla T=\alpha\cdot\nabla^2 T \tag{1a}$$

$$T(x,y,z,t=0)=T_{\mathrm{init}}(x,y,z) \tag{1b}$$

$$T(x,y,z,t)=0 \quad \text{on the walls} \tag{1c}$$

$$T(x=L_G,y,z,t)=e^{-cL_G}T(x=0,y,z,t) \tag{1d}$$

Equation 1(d) corresponds to the fully developed and periodic condition where the temperature profile is self-similar from one cell to the next, i.e., $T(x+L_G,y,z,t)=e^{-cL_G}\cdot T(x,y,z,t)$ for all (x,y,z,t), where $e^{-cL_G}=C$. The constant c is unknown and is a parameter to be determined as part of the computation. The fact that each cell independently satisfies the homogeneous Eq. (1) and that we are considering fully developed solutions that are independent of T_{init} implies that the solution to (1) for each cell would yield the same value of c. Hence, c cannot be a function of x. Moreover, it is readily demonstrated from energy arguments that, under fully developed conditions, c cannot be a function of time even when the flow is itself unsteady.

Any function satisfying the above self-similar condition has the unique decomposition $T(x,y,z,t)=e^{-cx}\theta(x,y,z,t)$, where $\theta(x+L_G,y,z,t)=\theta(x,y,z,t)$ is a periodic function. Thus, the computation of T is reduced to the computation of a periodic function θ, and the constant c. Substituting this decomposition into Eq.(1) yields

$$\frac{\partial\theta}{\partial t}+\overline{U}\cdot\nabla\theta-\alpha\cdot\nabla^2\theta=(\alpha\cdot c^2+uc)\theta-2\alpha\cdot c\frac{\partial\theta}{\partial x} \tag{2a}$$

$$\theta(x,y,z,t=0)=\theta_{\mathrm{init}}(x,y,z) \tag{2b}$$

$$\theta(x,y,z,t)=0 \quad \text{on the walls} \tag{2c}$$

$$\theta(x=L_G,y,z,t)=\theta(x=0,y,z,t). \tag{2d}$$

Since the fully developed solution is independent of the initial condition we may arbitrarily set $\theta_{\mathrm{init}}=1$. Equation (2*a*) is solved using a semi-implicit time-stepping procedure similar to that for our Navier-Stokes solver. The diffusive terms are treated implicitly while the convective terms are treated explicitly. In addition, all terms on the right of Eq. (2*a*) are treated explicitly using the latest available value for c. To avoid excessive time step restrictions, the diffusive terms are treated implicitly, while the convective terms are treated explicitly.

In the steady state case ($\partial/\partial t=0$), Eq. (2) constitutes an eigenproblem for the eigenpair (c,θ). The constant c corresponds to the decay rate of the mean temperature in the *x*-direction. As such, a larger value of c implies more rapid decay and more effective heat transfer. In the convection-dominated limit where the Peclet number U_aD_h/α is large, Eq. (2*a*) becomes a linear eigenvalue problem. In this case standard iterative methods for computing the

lowest value of c (corresponding to the most slowly decaying mode in x) can be used even when the nonlinear (c^2) term in Eq. (2a) is not identically zero. We find that this method accurately computes the decay rate and Nusselt numbers for steady flows in square and round ducts [22].

For steady periodic flows with period τ, the temperature is periodic in time, implying $T(x,y,z,t+\tau)=T(x,y,z,t)$. Since c is independent of time, this implies that $\theta(x,y,z,t+\tau)=\theta(x,y,z,t)$. If the value of c is not chosen correctly, this condition will not be satisfied. Unfortunately, τ is not known a priori but is a result of the hydrodynamic part of the calculation. A robust approach to compute c and θ is obtained by multiplying Eq. (2a) by θ, integrating over a single cell Ω, and simplifying to yield:

$$\frac{1}{2}\frac{d}{dt}\int_{\Omega}\theta^2 dV=\int_{\Omega}[(\alpha c^2+uc)\theta^2-\alpha\nabla\theta\cdot\nabla\theta]dV. \qquad (3)$$

While we do not expect the time derivative of the average temperature (represented by the left-hand side of Eq. (3)) to be identically zero, it will in general be less than the time derivative of θ at any one point in the domain. Moreover, if we integrate the right-hand side of Eq. (3) from time t to $t+\tau$, the resultant quantity must be zero due to the temporal periodicity.

This suggests a two-tier strategy for computing c in the unsteady case. Initially, we determine c such that the right hand side of Eq. (3) is identically zero at each time step. This will permit a relatively coarse but quick determination of c and θ. Subsequently, once τ is well established, we use this value of c to advance θ for one or more periods, and monitor the decay or growth of $\int\theta^2 dV$. At the end of each trial period, we adjust c until convergence is attained. Typical values of cL_G over the range of Re considered are 0.1039 to 0.1127, corresponding to 9.87 to 10.6 percent drops in mean temperature over a single groove length.

The periodic groove simulations were initialized using results from our work on contiguously grooved passages at Reynolds numbers of Re=405, 509, 640, and 764 [12]. To initialize the groove-flat computations, the periodic groove data was copied to the final groove, and plane Poiseuille flow of the same mass flux was used in the flat region. The combined simulations were then run for a sufficient length of time to flush the groove-flat region several times before collecting transport data.

The time and z-direction averaged temperature, velocity and pressure at each x,y-location are calculated after initial transients decay by averaging backwards from the final time t_F over successively longer intervals until the result converged. For example the average temperature field is

$$T_A(x,y)=\frac{1}{(t_F-t_1)W}\int_{t_l}^{t_F}\int_0^W T(x,y,z,t)dzdt.$$

In this expression t_l is a time after the flow has flushed through the domain several times but early enough so the results do not depend on its value.

The polynomial degree is $N=7$ for all calculations in this paper, corresponding to a grid point count of approximately 10^6. Our earlier work on contiguously grooved passages [11,12] established that $N=7$ and 9 give the same heat transfer and pressure gradient results at Re=950. Since the size of the smallest flow structures *increase* as the Reynolds number decreases, the results for Re<950 with $N=7$ were assumed to be spatially resolved and insensitive to higher spectral orders. Moreover, since the maximum Reynolds number for the current study is Re=764 there is no reason to believe that the current geometry contains smaller structures than the ones found in the earlier work. No additional spectral order sensitivity analysis was therefore seen as necessary for this geometry.

Our earlier work for a fully developed grooved channel used periodic boundary conditions in the z-direction and a domain width of $W=2$ cm [12]. That work showed that the transport results at Re=500 were not sensitive to the use of a wider domain ($W=3$ cm). The results for Re≥500 were assumed to be insensitive to the use of wider domains since the dominant flow modes were expected to *decrease* in size with increasing Reynolds numbers.

The domain width of $W=2$ cm was also used in the current study because it is twice the minimum wall-to-walls spacing H. However, due to the very large number of grid points and long time integrations involved in the current calculation, computational resources were not available to conduct a domain-width sensitivity study. This is unfortunate since the lowest Reynolds number of the current work (Re=405) is less than the value at which the width sensitivity analysis was performed in our earlier work. Moreover, small eddy structures exiting the grooved domain may possibly coalesce into larger structures as they move in the flat passage. However, the simulations at Re=509, 640, and 764 (Fig. 2) predict that the most energetic (most slowly decaying) structures have z-dimensions that are half the passage width or less.

The simulations were performed on $P=8$, 16, 32, and 64 processors of a 96 processor SGI Origin 2000. Each processor is a MIPS R10000 running at 250 MHz and shares 24 GB of memory. A typical three-dimensional simulation requires approximately fourteen seconds per time step ($\Delta t=0.00005$) for the groove ($P=16$) and for the groove-flat ($P=64$) simulations. The groove and groove-flat simulations were run concurrently with the outflow data from the groove used as the inflow boundary condition data of the groove-flat simulation.

Results

Velocity. Figure 2 shows the v-component of velocity in the passage center plane ($y=H/2$). These surfaces represent typical snapshots at four Reynolds numbers, Re=405, 509, 640, and 764. In this work the Reynolds number is $\mathrm{Re}=U_m D_H/\nu$, where the average velocity through the minimum channel cross section is $U_m=Q/WH$, the minimum channel hydraulic diameter is $D_H=2H$, ν is the fluid kinematic viscosity, and Q is the volume flow rate passing through the domain. The results in Fig. 2 are from the groove-flat sub-domain shown in Fig. 1(b).

Studies of transversely grooved passages have shown that Kelvin-Helmholtz instabilities of shear layers that span the groove openings destabilize two-dimensional Tollmien-Schlichting waves at Re=350 [2], and that three-dimensional flow structures develop as the Reynolds number increases [9]. Figure 2 shows that at Re=405 two-dimensional waves (with essentially no variation in the z-direction) travel through the groove region and decay downstream. At Re=509, the flow is three-dimensional with regular variations in the z-direction. This variation is much less regular as the Reynolds number increases to Re=640 and 764. Careful examination of the downstream edge of the surfaces at Re=509, 540, and 764 show that the most slowly decaying modes have two waves in the z-direction. Disturbances in flat passage flows generally decay for Reynolds numbers less than Re=2800 [23]. We see that unsteady flow structures that develop in the grooved regions dissipate in the flat section for all four Reynolds numbers considered in this work.

Figure 3 shows the unsteady component of fluid speed S_{rms} versus axial position and Reynolds number at the channel center plane ($y=H/2$). This unsteady speed is $S_{\mathrm{rms}}=(u_{\mathrm{rms}}^2+v_{\mathrm{rms}}^2+w_{\mathrm{rms}}^2)^{1/2}$ where u_{rms}, v_{rms}, and w_{rms} are the root mean squared averaged deviations of the x- and z-components of velocity from their respective mean values. In Fig. 3, S_{rms} is normalized by the fully developed centerline velocity in a parallel plate passage, $U_{p,c}=1.5U_m$. The region $0\leq x/L_G\leq 1$ represents results from the periodic groove domain (Fig. 1(a)). The region $1\leq x/L_G\leq 2$ corresponds to the groove portion of the groove-flat domain, referred to as the "last groove." The region $2\leq x/L_G\leq 7$ represents the flat section.

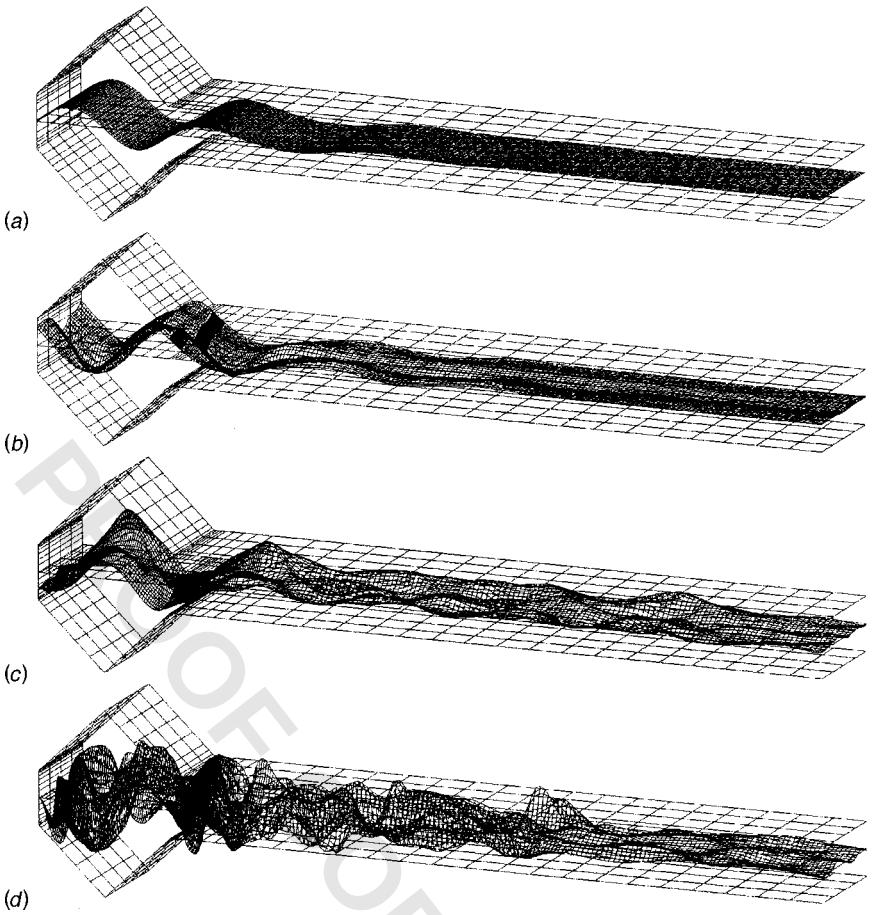

Fig. 2 Surfaces of *v*-velocity at $y=H/2$. (*a*) Re=405. (*b*) Re=509. (*c*) Re=640. (*d*) Re=764.

We see that the level of unsteadiness in the grooves increases from roughly 8 percent at Re=405 to over 16 percent at Re=764. At each Reynolds number the profile shapes in the two grooves are similar. However, the values in the downstream three-quarters of the last groove ($x/L_G=1.25$ to 2) are somewhat different than those in the periodic groove ($x/L_G=0.25$ to 1). This is an elliptic effect caused by the presence of the downstream flat passage.

The unsteadiness that develops in the grooved regions dissipates in the flat section for all four Reynolds numbers, as discussed in connection with Fig. 2. The rate of axial decay is steep near $x/L_G=2$ and then decreases further downstream. At Re =405, the unsteadiness decays to essentially zero before the end of the flat passage. At the higher Reynolds numbers, however, unsteadiness is still present five groove-lengths after the end of the grooved passage.

Figure 4 is a plot of time average velocity in the channel center plane U_c versus axial position. This velocity is normalized by the fully developed centerline velocity in a parallel plate passage, $U_{p,c}$. Once again, while the profile shapes are similar in the two grooves, the flat passage does affect the centerline velocity in the downstream three-quarters of the last groove. We see that the centerline velocity experiences a substantial acceleration near $x/L_G=2$. This acceleration is caused by the development of boundary layers on the surfaces of the flat region. For Re=405 the

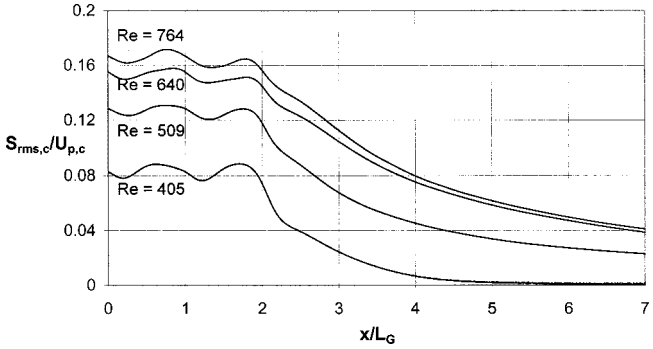

Fig. 3 Centerline unsteady velocity versus location and Reynolds number.

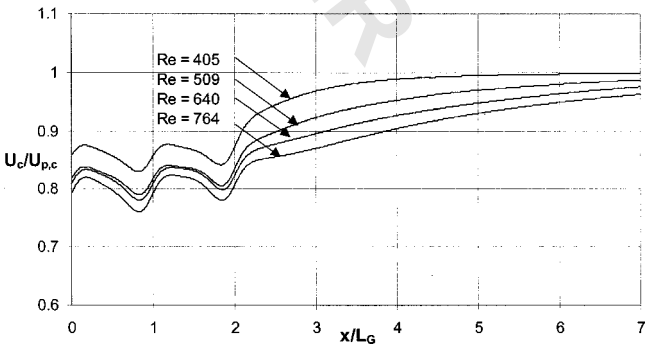

Fig. 4 Centerline velocity versus axial location and Reynolds number

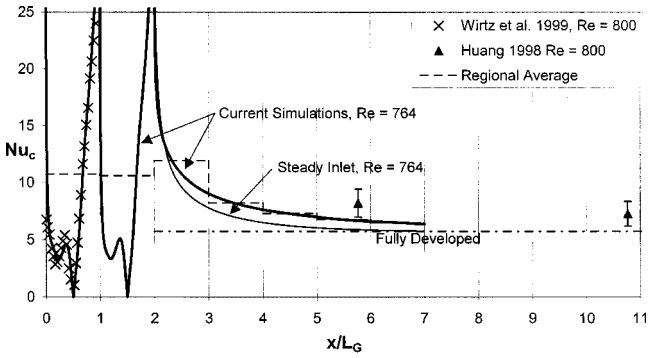

Fig. 5 Centerline Nusselt number versus axial location

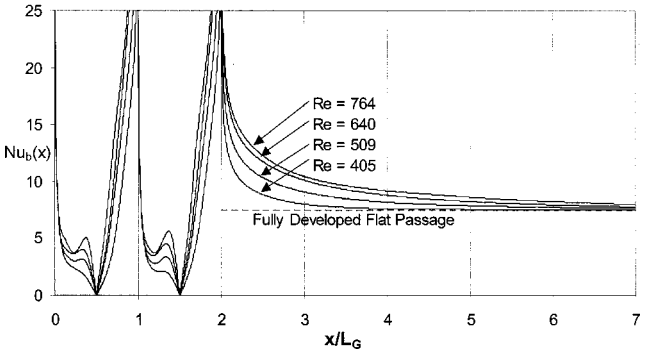

Fig. 6 Bulk Nusselt number versus axial location

centerline speed reaches the flat passage fully developed value at $x/L_G=7$. For higher Reynolds number however, the centerline speed does not reach the fully developed value before the end of the computational domain. Finally, comparing the profiles of average centerline velocity in Fig. 4 with the rms profiles in Fig. 3, we see that regions of accelerating flow ($dU_c/dx>0$) generally correspond to regions of rapidly decreasing unsteadiness ($dS_{\rm rms}/dx<0$).

Transport. Figure 5 shows measured and calculated centerline Nusselt numbers Nu_C versus axial position. The centerline Nusselt number is defined as $\mathrm{Nu}_C=q''D_h/(\Delta T_C k)$. In this expression the heat transfer to the fluid per unit *projected* surface area is $q''=-k(dT_A/dn)_{\rm wall}/m$, where T_A is the time and z-averaged temperature, n is the direction normal to the wall, m is the wall surface direction cosine, and the temperature gradient is evaluated at the wall. The direction cosine in the flat region is $m=1$, while it is $m=0.7071$ in the grooved region. The fluid thermal conductivity is k, and ΔT_C is the local, time and z-averaged difference between the surface temperature and the fluid temperature at the *centerline* of the passage $T_A(y=H/2)$ (rather than the bulk fluid temperature). The holographic measurement technique used in the experiments was better suited for measuring local centerline temperatures than it was for measuring bulk values [10,16].

Measurements made in a fully developed grooved channel at $\mathrm{Re}=800\pm57$ (the reported uncertainly limit has a 99 percent confidence level) are shown using x-symbols [16]. Measurements in a flat passage downstream from the groove channel at the same Reynolds number are shown using up-pointing triangles [10]. The 99 percent confidence level uncertainty limits on the flat passage measurements are shown using error bars. Directly comparable center point Nusselt numbers calculated from the current simulation at $\mathrm{Re}=764$ are shown using a heavy solid line (the value $\mathrm{Re}=764$ was used so that the simulation could be initiated using earlier results from a fully developed groove passage simulation [12]. The thinner solid line is from a simulation that used steady inlet temperature and velocity profiles at $x/L_G=2$. Those profiles were equal to the time average profiles from the unsteady simulations at $\mathrm{Re}=764$. Horizontal dashed lines represent arithmetic average values of Nu_C in the regions $0\leqslant x/L_G\leqslant 1$, $1\leqslant x/L_G\leqslant 2$, $2\leqslant x/L_G\leqslant 3$, etc. A dashed-dot line shows the fully developed center point Nusselt number for a laminar flat channel.

The experimental measurements in a fully developed groove show that the heat transfer on the downstream (windward) surface ($0.5\leqslant x/L_G\leqslant 1$) is significantly higher than the heat transfer on the upstream (leeward) side ($0\leqslant x/L_G\leqslant 0.5$). This is due to the direction of the re-circulating vortex flow in the groove. The upstream surface exhibits a local peak at $x/L_G=0.3$ due to the impingement of the vortex at that location. The experimental results in the flat passage show that the heat transfer is at least 25 percent higher than the fully developed flat passage value for $x/L_G<11$.

Figure 5 shows excellent agreement between the experimental and numerical results in the periodically fully developed grooved channel ($0\leqslant x/L_G\leqslant 1$). However, the numerical results decay more rapidly in the flat region than is expected from the measurements. We do not currently understand why this difference exists.

We note that while the numerical Nusselt number profile in the last groove ($1\leqslant x/L_G\leqslant 2$) has a different shape from that in the fully developed groove ($0\leqslant x/L_G\leqslant 1$), the regionally averaged values for these two grooves (horizontal dashed lines) are roughly equal. The average heat transfer over the first groove-length of the flat passage ($2\leqslant x/L_G\leqslant 3$) is somewhat larger than value in the groove regions. Subsequent regionally averaged values decrease as distance from the last groove increases. Finally, we note that the simulation that used steady inlet conditions at $x/L_G=2$ (thinner solid line) gave a Nusselt number profile that is roughly 20 percent below the results from the unsteady simulation. We see that at this Reynolds number, unsteadiness from the grooved channel increases the flat passage heat transfer for at least five groove-lengths.

Figure 6 shows local *bulk* Nusselt number versus axial location for $405\leqslant\mathrm{Re}\leqslant 764$. The bulk Nusselt number is defined as $\mathrm{Nu}_B=q''D_h/(\Delta T_B k)$, where ΔT_B is the local, time averaged difference between the surface and bulk fluid temperatures. The bulk temperature at any axial location x and time t is defined as $T_B(x,t)=(\int uTdA)/(\int udA)$, where both integrations are taken across the entire cross sectional area at the given x-location.

We see that the heat transfer level throughout the domain increases with Reynolds number. In the grooved region, the local peak heat transfer due to impingement of the vortices becomes more prominent with increasing Re. Moreover, while the Nusselt number profiles in the two grooves are similar, the local maximum is more prominent in the last groove than it is in the periodic groove. In the flat region, the Nusselt number is very high at the inlet and drops off in the axial direction. These Nusselt number values approach the value of a fully develop flat channel for large x/L_G. However, the decay rate decreases as the Reynolds number increases.

Figure 7 shows the log mean bulk Nusselt number versus Reynolds number and location. Each line represents a different region in the passage. The log mean Nusselt number is defined as $\mathrm{Nu}_{B,LM}=qR\prime\prime D_h/(\Delta T_{B,LM}k)$, where $\Delta T_{B,LM}$ is the log mean bulk temperature difference across each region, and q''_R is the total heat flux to the region divided by its total projected surface area. The fully develop bulk Nusselt number for a flat passage is shown using a dashed line.

The log mean Nusselt numbers in the periodic groove region (open squares) and the final groove (x-symbols) are essentially identical for all four Reynolds numbers considered in this work. At $\mathrm{Re}=405$, the heat transfer coefficient in the groove region is actually lower than the level in a flat passage. The thermal resistance of the slowly turning groove vortices causes this. Even though the flow field is unsteady at this Reynolds number (see Figs. 2(a) and 3), the level of enhanced mixing is not sufficient to

PROOF COPY 011201JHR

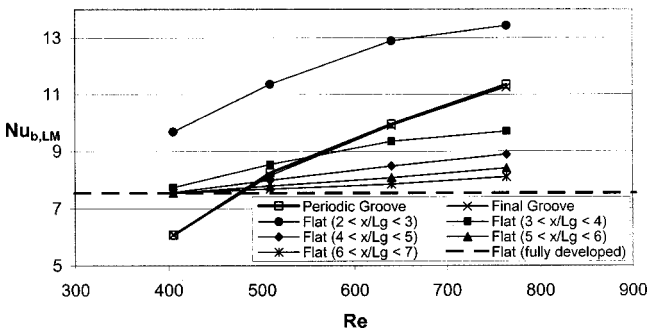

Fig. 7 Regionally averaged Nusselt number versus Reynolds number and location

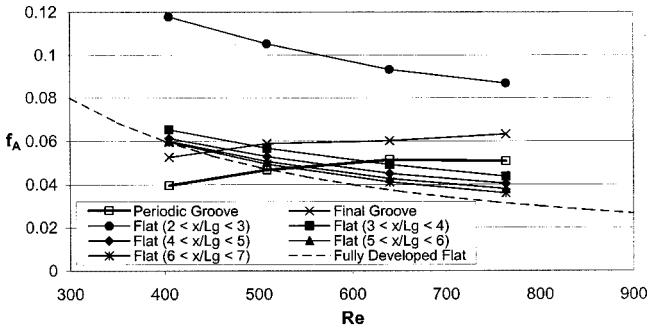

Fig. 9 Regionally averaged pressure gradient versus Reynolds number and location

overcome this resistance. At Re=509, the level of three dimensional mixing exhibited in Figs. 2(*b*) and 3 is sufficient to slightly overcome the thermal resistance of the grooves. As the Reynolds number is increased to Re=640 and 764, the highly irregular three-dimensional mixing discussed earlier substantially increases heat transfer compared to a flat passage.

In the first groove-length of the flat passage ($2 \leqslant x/L_G \leqslant 3$, solid circles) the average heat transfer exceeds the grooved channel value for all Reynolds numbers considered. This increased heat transfer is due to the absence of the thermal resistance of the groove. The heat transfer decreases in each subsequent region and eventually approaches the fully developed flat passage value.

Figure 8 shows the local dimensionless pressure gradient f versus axial location and Reynolds number. The dimensionless gradient is defined as $f=(-dp_{A,c}/dx)[D_h/(2\rho U_m^2)]$, where $p_{A,c}$ is the time and z-averaged pressure in the center plane ($y=H/2$) and ρ is the fluid density. The profiles of f are in many ways similar in shape to the Nusselt number profiles seen in Fig. 6. However, while the Nusselt number profile represents the heat flux (temperature gradient) at the wall, the pressure gradient is a combination of wall shear stress (velocity gradient) and the axial gradient of the momentum flux. The converging and diverging regions of the grooved sections, as well as the developing boundary layer flow in the flat passage, cause the velocity profiles to vary in the axial direction. This variation may cause the axial gradient of the momentum flux to be significant.

The pressure gradient profiles in the two grooves are similar to each other. However, the flat passage affects the pressure gradient in the downstream three-quarters of the last groove. The pressure gradient at $x/L_G=2$ is substantially greater than the value at $x/L_G=1$. This is due to the acceleration of the flow at $x/L_G=2$, discussed in connection with Fig. 4.

Figure 9 shows the average dimensionless pressure gradient across different regions of the passage versus Reynolds number and location. The average gradient is defined as

$$f_A=\frac{1}{x_2-x_1}\int_{x_1}^{x_2} f\,dx=\frac{p_{A,1}-p_{A,2}}{x_2-x_1}\,\frac{D_h}{2\rho U_m^2},$$

where $p_{A,1}$ and $p_{A,2}$ are the time and z-average centerline pressures at locations x_1 and x_2, respectively. Each line corresponds to the average across a different region in the passage ($0 \leqslant x/L_G \leqslant 1$, $1 \leqslant x/L_G \leqslant 2$, $2 \leqslant x/L_G \leqslant 3$, etc). A dashed line shows the fully developed Fanning friction factor for a flat passage ($f=24/\mathrm{Re}$).

The dimensionless pressure gradient across the periodic groove (open squares in Fig. 9) increases with Reynolds number. At Re =405, this pressure gradient is actually smaller than the gradient in a flat passage. This is because the grooves effectively relax the no slip boundary conditions at $y=0$ and H. While the flow is unsteady at this Reynolds number, the level of mixing does not overcome the decrease in drag due to the grooves. As the Reynolds number increases to Re=509, the flow exhibits three dimensional mixing that brings the pressure gradient in the periodic groove to the same value as a flat passage. The pressure gradient increases beyond the level in flat passages at higher Reynolds numbers.

Unlike the heat transfer, the pressure gradient across the last groove is substantially larger than that across the periodic groove. This is partially due to the acceleration of the flow as it enters the flat passage. The dimensionless pressure gradient reaches its highest values in the first groove-length of the flat passage ($2 \leqslant x/L_G \leqslant 3$) and rapidly drops back to the fully developed flat passage values further downstream.

Figure 10 is a plot of the log mean bulk Nusselt number for different regions of the passage versus the dimensionless power required to pump fluid through the region. The dimensionless pumping power per unit length is

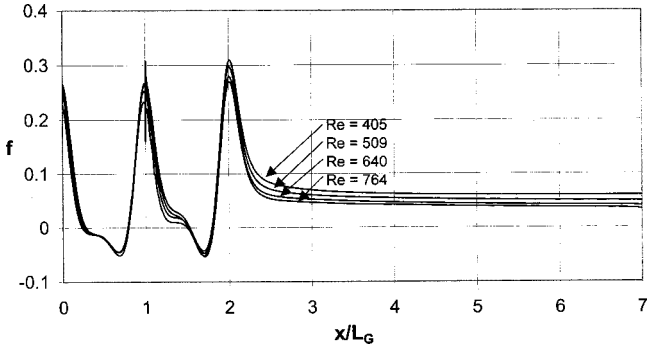

Fig. 8 Local dimensionless pressure gradient versus axial location and Reynolds number

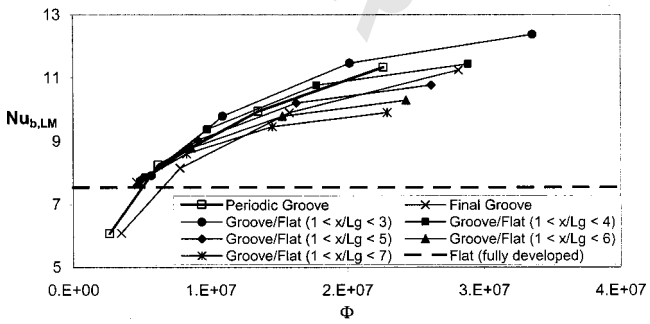

Fig. 10 Regionally averaged Nusselt number versus pumping power

$$\Phi = \frac{p_{A,1} - p_{A,2}}{x_2 - x_1} \frac{Q}{W} \frac{D_h^3}{\rho \nu^3} = f_A \, \mathrm{Re}^3$$

In Fig. 10, different lines are used for the periodic groove (heavy line with open squares), the last groove (*x*-symbols), and regions that include the last groove *and* different lengths of the flat passage (i.e., $2 \leqslant x/L_G \leqslant 3$, $2 \leqslant x/L_G \leqslant 3$, etc.). The horizontal dashed line shows the performance of a fully developed flat passage. The purpose of this plot is to compare the performance of flat regions downstream from a fully developed grooved passage to the performance of the grooved passage itself. The last groove is included with the flat passage because the flat region always affects its performance.

The results for the fully developed groove (open squares) show that the heat transfer increases with the pumping power. Heat transfer in laminar parallel plate flow, on the other hand, is constant. Moreover, the curvature of this line indicates that at low pumping power levels, small increases in pumping power lead to large increases in heat transfer. However, the increase in heat transfer for a given increase in pumping power diminishes as the initial pumping power level increases. The final groove (*x*-symbols) gives lower levels of heat transfer for a given pumping power than in the fully developed groove. This is because the heat transfer levels in the two grooved regions are the same but the pressure gradient in the last groove is higher than that in the fully developed groove.

For the region that includes the last groove and the first groove-length of the flat passage (solid circles), the heat transfer for a given pumping power is roughly 5 percent higher than that in the fully developed groove. Alternately stated, the pumping power requirement for a given heat transfer level is decreased by approximately 25 percent. As the flat region length increases, its performance approaches that of a fully developed flat passage and its average heat transfer decreases. However, configurations with flat regions up to three groove-lengths long still exhibit higher heat transfer for a given pumping power than a fully developed grooved passage.

Conclusions

Navier-Stokes simulations of three-dimensional flow and augmented convection in a flat passage downstream from a fully developed channel with symmetric, transverse grooves on two opposite walls were performed for $405 \leqslant \mathrm{Re} \leqslant 764$ using the spectral element technique. Unsteady flow that develops in the grooved region persists several groove-lengths into the flat passage, increasing both local heat transfer and pressure gradient relative to steady flat passage flow. Moreover, the heat transfer for a given pumping power in a flat region up to three groove-lengths long is even greater than the high levels observed in a fully developed grooved passage.

This work suggests that the performance of intermittently grooved passages, in which flat regions separate contiguously grooved sections, may offer favorable heat transfer versus pumping power performance in engineering devices. However, the development of unsteady flow in short grooved regions and the decay of non-fully-developed grooved channel unsteadiness in flat regions must be investigated before these designs can be optimized [24,25].

Acknowledgments

National Science Foundation Grant CTS-9501502 supported this work. The work of P. F. Fischer was supported by the Mathematical, Information, and Computational Sciences Division subprogram of the Office of Advanced Scientific Computing Research, U.S. Department of Energy, under Contract W-31-109-Eng-38. The work of H. M. Tufo was supported by the Department of Energy under Grant number B341495 to the Center on Astrophysical Thermonuclear Flashes at University of Chicago, and by the University of Chicago.

Nomenclature

b = groove depth, Fig. 1
L_G = channel periodicity length, Fig. 1
c = decay constant
D_h = minimum hydraulic diameter, $2H$
f = fanning friction factor, $(dp/dx)[f_x/(2\rho U_a^2)]$
f_x = fluid body force per unit mass in the *x*-direction
H = minimum channel wall to wall spacing, Fig. 1
k = fluid thermal conductivity, 0.0263 W/m°C
K = number of spectral elements
N = spectral element order
Nu_b = bulk Nusselt number based on projected area
Nu_c = center point Nusselt number
Pr = fluid molecular Prandtl number, 0.70
Re = Reynolds number, $U_m D_h / \nu$
t = time
T = temperature
T_b = bulk temperature
T_c = center point temperature
u,v,w = velocity components in the *x*, *y*, and *z* directions
U_m = mean *x*-velocity at the minimum channel cross-section
V = volume
Q = volume flow rate, $V_r = (1/L)\int_\Omega u dV$
W = width of the computational domain, Fig. 1

Greek

α = thermal diffusivity, 2.63×10^{-5} m^2/s
ν = fluid kinematic viscosity, 1.84×10^{-5} m^2/s
θ = periodic temperature
ρ = fluid density, 1.006 kg/kg
τ = period of local time variations
Ω = computation domain

References

[1] Webb, R. L., 1994, *Principles of Enhanced Heat Transfer*, John Wiley & Sons, New York.
[2] Ghaddar, N. K., Korczak, K., Mikic, B. B., and Patera, A. T., 1986, "Numerical Investigation of Incompressible Flow in Grooved Channels: Part 1—Stability and Self-Sustained Oscillations," J. Fluid Mech., **168**, pp. 541–567.
[3] Greiner, M., 1991, "An Experimental Investigation of Resonant Heat Transfer Enhancement in Grooved Channels," Int. J. Heat Mass Transf., **24**, pp. 1383–1391.
[4] Roberts, E. P. L., 1994, "A Numerical and Experimental Study of Transition Processes in an Obstructed Channel Flow," J. Fluid Mech., **260**, pp. 185–209.
[5] Kozlu, H., Mikic, B. B., and Patera, A. T., 1988, "Minimum-Dissipation Heat Removal by Scale-Matched Flow Destabilization," Int. J. Heat Mass Transf., **31**, pp. 2023–2032.
[6] Karniadakis, G. E., Mikic, B. B., and Patera, A. T., 1988, "Minimum-Dissipation Transport Enhancement by Flow Destabilization: Reynolds Analogy Revisited," J. Fluid Mech., **192**, pp. 365–391.
[7] Amon, C. H., Majumdar, D., Herman, C. V., Mayinger, F., Mikic, B. B., and Sekulic, D. P., 1992, "Experimental and Numerical Investigation of Oscillatory Flow and Thermal Phenomena in Communicating Channels," Int. J. Heat Mass Transf., **35**, pp. 3115–3129.
[8] Greiner, M., Chen, R.-F., and Wirtz, R. A., 1989, "Heat Transfer Augmentation Through Wall-Shaped-Induced Flow Destabilization," ASME J. Heat Transfer, **112**, pp. 336–341.
[9] Greiner, M., Chen, R.-F., and Wirtz, R. A., 1991, "Enhanced Heat Transfer/Pressure Drop Measured From a Flat Surface in a Grooved Channel," ASME J. Heat Transfer, **113**, pp. 498–500.
[10] Wirtz, R. A., Huang, F., and Greiner, M., 1999, "Correlation of Fully Developed Heat Transfer and Pressure Drop in a Symmetrically Grooved Channel," ASME J. Heat Transfer, **121**, pp. 236–239.
[11] Greiner, M., Spencer, G., and Fischer, P. F., 1998, "Direct Numerical Simulation of Three-Dimensional Flow and Augmented Heat Transfer in a Grooved Channel," ASME J. Heat Transfer, **120**, pp. 717–723.
[12] Greiner, M., Faulkner, R. J., Van, V. T., Tufo, H. M., and Fischer, P. F., 2000, "Simulations of Three-Dimensional Flow and Augmented Heat Transfer in a Symmetrically Grooved Channel," ASME J. Heat Transfer, **122**, pp. 653–660.
[13] Blair, M. F., 1983, "Influence of Free-Stream Turbulence on Turbulent Bound-

ary Layer Heat Transfer and Mean Profile Development: Part I—Experimental Data; Part II—Analysis of Results,'' ASME J. Heat Transfer, **105**, pp. 33–47.
[14] Maciejewski, P. K., and Moffat, R. J., 1992, ''Heat Transfer with Very High Free-Stream Turbulence: Part I—Experimental Data; Part II—Analysis of Results,'' ASME J. Heat Transfer, **114**, pp. 827–839.
[15] Greiner, M., Chen, R.-F., and Wirtz, R. A., 1995, ''Augmented Heat Transfer in a Recovery Passage Downstream From a Grooved Section: An Example of Uncoupled Heat/Momentum Transport,'' ASME J. Heat Transfer, **117**, pp. 303–308.
[16] Huang, F., 1998, ''Experimental Investigation of Fully-Developed Augmented Convection in a Symmetrically Grooved Channel,'' Masters of Science Degree thesis, University of Nevada, Reno.
[17] Patera, A. T., 1984, ''A Spectral Element Method for Fluid Dynamics; Laminar Flow in a Channel Expansion,'' J. Comput. Phys., **54**, pp. 468–488.
[18] Maday, Y., and Patera, A. T., 1989, ''Spectral Element Methods for the Navier-Stokes Equations,'' *State of the Art Surveys on Computational Mechanics*, A. K. Noor and J. T. Oden, eds., ASME, New York, pp. 71–143.
[19] Fischer, P. F., 1997, ''An Overlapping Schwarz Method for Spectral Element Solution of the Incompressible Navier-Stokes Equations,'' J. Comput. Phys., **133**, pp. 84–101.
[20] Fischer, P. F., and Patera, A. T., 1992, ''Parallel Spectral Element Solutions of Eddy-Promoter Channel Flow,'' *Proceedings of the European Research Community on Flow Turbulence and Computation Workshop*, Lausanne, Switzerland, Cambridge University Press, pp. 246–256.
[21] Patankar, S. V., Liu, C. H., and Sparrow, E. M., 1977, ''Fully Developed Flow and Heat Transfer in Ducts Having Streamwise Periodic Variations of Cross-Sectional Area,'' ASME J. Heat Transfer, **99**, pp. 180–186.
[22] Kays, W. M., and Crawford, M. E., 1993, *Convection Heat and Mass Transfer*, Third Edition, McGraw-Hill, New York.
[23] Fox, R. W., and McDonald, A. T., 1985, *Introduction to Fluid Mechanics*, 3rd Edition, John Wiley & Sons, New York, p. 338.
[24] Fischer, P. F., and Patera, A. T., 1991, ''Parallel Spectral Element Solutions of the Stokes Problem,'' J. Comput. Phys., **92**, pp. 380–421.
[25] Fischer, P. F., and Ronquist, E. M., 1994, ''Spectral Element Methods for Large Scale Parallel Navier-Stokes Calculations,'' Comp. Meth. Mech. Engr., ■■, pp. 69–76.

PROOF COPY 011201JHR